AFRL-RY-WP-TP-2021-0176

STATISTICAL ANALYSIS OF SAL MODEL-BASED ATMOSPHERIC PHASE CORRECTION ALGORITHM (Preprint)

Randy S. Depoy Jr.

LADAR Technology Branch
Multispectral Sensing & Detection Division

Arnab K. Shaw

Wright State University

JULY 2021
Final Report

AIR FORCE RESEARCH LABORATORY
SENSORS DIRECTORATE
WRIGHT-PATTERSON AIR FORCE BASE, OH 45433-7320
AIR FORCE MATERIEL COMMAND
UNITED STATES AIR FORCE

REPORT DOCUMENTATION PAGE

Form Approved
OMB No. 0704-0188

1. REPORT DATE *(DD-MM-YY)*	2. REPORT TYPE	3. DATES COVERED *(From - To)*
July 2021	Journal Article Preprint	29 June 2021 –29 June 2021

4. TITLE AND SUBTITLE
STATISTICAL ANALYSIS OF SAL MODEL-BASED ATMOSPHERIC PHASE CORRECTION ALGORITHM (Preprint)

5a. CONTRACT NUMBER
N/A

5b. GRANT NUMBER

5c. PROGRAM ELEMENT NUMBER
N/A

6. AUTHOR(S)
Randy S. Depoy Jr. (AFRL/RYMM)
Arnab K. Shaw (Wright State University)

5d. PROJECT NUMBER
N/A

5e. TASK NUMBER
N/A

5f. WORK UNIT NUMBER
N/A

7. PERFORMING ORGANIZATION NAME(S) AND ADDRESS(ES)

Air Force Research Laboratory
Sensors Directorate (AFRL/RYMM)
Wright-Patterson Air Force Base, OH 45433-7320
Air Force Materiel Command
United States Air Force

Wright State University

8. PERFORMING ORGANIZATION REPORT NUMBER

9. SPONSORING/MONITORING AGENCY NAME(S) AND ADDRESS(ES)

Air Force Research Laboratory
Sensors Directorate
Wright-Patterson Air Force Base, OH 45433-7320
Air Force Materiel Command
United States Air Force

10. SPONSORING/MONITORING AGENCY ACRONYM(S)
AFRL/RYMM

11. SPONSORING/MONITORING AGENCY REPORT NUMBER(S)
AFRL-RY-WP-TP-2021-0176

12. DISTRIBUTION/AVAILABILITY STATEMENT
DISTRIBUTION STATEMENT A. Approved for public release; distribution is unlimited.

13. SUPPLEMENTARY NOTES
PAO case number AFRL-2021-2032, Clearance Date 29 June 2021. The U.S. Government is joint author of this work and has the right to use, modify, reproduce, release, perform, display, or disclose the work. Report contains color.

14. ABSTRACT

Synthetic Aperture Ladar (SAL) is an emerging ladar remote sensing technology based on the well-established synthetic aperture sensing techniques, such as Synthetic Aperture Radar (SAR). A SAL sensor operates at optical instead of RF wavelengths. A key benefit of the reduction in wavelength is SAL sensor's collect phase history data with an equivalent resolution to SAR in 10,000× shorter time. A key technical challenge limiting the efficacy of a SAL sensor is atmospheric turbulence. Advanced algorithms to mitigate atmospheric phase errors in measured SAL data are necessary to obtain the desired interpretable imagery when the atmosphere is the limiting factor in performance. In this paper, we conduct statistical performance analysis of a recently proposed algorithm known as the model-based atmospheric phase correction (MBAPC) and validate it using Monte Carlo simulations. Specifically, we derive the Cramer-Rao Lower Bound (CRLB) for the estimate of the unknown atmospheric model parameter. We show that the MBAPC algorithm asymptotically attains the CRLB as it is the maximum-likelihood estimator (MLE) under the assumption of additive complex white Gaussian noise (CWGN).

15. SUBJECT TERMS
non-visual features, overlap function, autofocusing, model-base image reconstruction, synthetic aperture ladar

16. SECURITY CLASSIFICATION OF:			17. LIMITATION OF ABSTRACT:	18. NUMBER OF PAGES	19a. NAME OF RESPONSIBLE PERSON (Monitor)
a. REPORT	b. ABSTRACT	c. THIS PAGE			Randy Depoy
Unclassified	Unclassified	Unclassified	SAR	14	19b. TELEPHONE NUMBER *(Include Area Code)* N/A

Statistical analysis of SAL model-based atmospheric phase correction algorithm

Randy S. Depoy Jr., Ph.D.*, Arnab K. Shaw, Ph.D.†
*Air Force Research Laboratory 3109 Hobson Way, WPAFB, OH 45433
Email: depoy.2@wright.edu
†Wright State University 3640 Colonel Glenn Hwy, Dayton, OH 45435
Email: arnab.shaw@wright.edu

***Abstract*—Synthetic Aperture Ladar (SAL) is an emerging ladar remote sensing technology based on the well-established synthetic aperture sensing techniques, such as Synthetic Aperture Radar (SAR). A SAL sensor operates at optical instead of RF wavelengths. A key benefit of the reduction in wavelength is SAL sensor's collect phase history data with an equivalent resolution to SAR in 10,000× shorter time. A key technical challenge limiting the efficacy of a SAL sensor is atmospheric turbulence. Advanced algorithms to mitigate atmospheric phase errors in measured SAL data are necessary to obtain the desired interpretable imagery when the atmosphere is the limiting factor in performance. In this paper, we conduct statistical performance analysis of a recently proposed algorithm known as the model-based atmospheric phase correction (MBAPC) and validate it using Monte Carlo simulations. Specifically, we derive the Cramer-Rao Lower Bound (CRLB) for the estimate of the unknown atmospheric model parameter. We show that the MBAPC algorithm asymptotically attains the CRLB as it is the maximum-likelihood estimator (MLE) under the assumption of additive complex white Gaussian noise (CWGN).**

I. Introduction

Synthetic aperture ladar (SAL) is an emerging ladar remote sensing technology based on the well-established sensing technique of synthetic aperture radar (SAR) [1]–[4]. In a spotlight-mode SAL collection the sensor platform traverses a straight and level flight path while an on-board ladar sensor collects data. The ladar sensor regularly transmits a linear frequency modulated (LFM) optical field to illuminate targets in a region-of-interest. Propagation of the optical field through a turbulent atmosphere imparts a log-amplitude and phase perturbation that varies across the optical field [5]–[7]. The perturbed optical field interacts with targets in the scene and a fraction of perturbed field reflects back to the receive aperture where it is detected with an optical dechirp-on-receive. A sampled version of the detected signal produces phase history data that can be coherently processed into imagery with a desired cross-range resolution exceeding the diffraction limit of the ladar [8]–[10].

SAL sensors are more susceptible to atmospheric effects that result from changes in the index-of-refraction at optical wavelengths. The transmitted LFM optical field propagates through the turbulent atmosphere which imparts phase perturbations corresponding to changes in the index-of-refraction. Propagation of the phase perturbed field results in self-interference of the field and produces log-amplitude and phase perturbations across the optical field [6], [7]. As the sensor platform traverses the synthetic aperture the atmospheric channel will change resulting in a slightly different atmospheric perturbation. The atmospheric perturbations imparted on a target's reflectivity vary spatially throughout the illuminated scene and as a function of synthetic aperture position [5]. As a result, the complex reflectivity of each target in the scene is no longer modeled as an isotropic scattering center [5], [11], [12]. In this paper we focus primarily on mitigating the atmospheric phase perturbations imparted by the atmosphere.

In order to achieve a desired cross-range resolution we must be able to coherently process the measured phase history data [8]–[10]. To coherently process the SAL data we must have accurate knowledge of the collection. Any deviations from the pre-determined collection will manifest as an error source on the measured signal that must be mitigated to restore coherence. Phase errors arise in measured SAL phase history data from a myriad of sources, such as, uncompensated motion errors, vibrations, and atmospheric turbulence [4], [5], [8]–[11]. We focus primarily on atmospheric phase errors.

The effects of phase errors on image quality are well established throughout the literature: Constant and linear phase errors result in undetectable shifts of a target in the spatial domain. Quadratic phase errors result in a broadening of the main-lobe of the SAL's point spread function (PSF). Higher frequency phase errors induce higher side-lobe levels in the cross-range dimension [8]–[10]. Atmospheric phase errors manifest as a power-law random process with a majority of the power concentrated on the lower frequency phase error components. As the turbulence strength increases higher frequency components become more significant and lead to a drastic decrease in image quality [5]–[7].

In order to improve the image quality we must estimate and remove the phase errors corrupting the phase history data using autofocus algorithms. The Phase Gradient Autofocus (PGA) algorithm is a well-established autofocusing algorithm in both the SAR and SAL literature. PGA iteratively estimates and removes phase errors from phase history data using the maximum-likelihood estimation kernel [13], [14]. The SAL community has explored the efficacy of PGA under a myriad of different operating conditions, each showing that PGA is an extremely useful autofocusing algorithm [15]–[18]. Another class of autofocusing algorithms implement an Image Quality Metric (IQM) optimization algorithm typically guided by an

analytical gradient [10], [19]–[22]. The IQM autofocusing algorithms arrive at the optimal estimate of the phase error in terms of image quality: sharpness, entropy, or contrast.

In addition to the aforementioned autofocus algorithms, there are a class of algorithms that estimate and incorporate unknown phase errors into iterative model based reconstruction algorithms [23]–[30]. The model based reconstruction algorithms rely on an accurate collection or model matrix to reconstruct a high quality imagery from measured phase history data. When the model matrix is corrupted by an unknown phase error the algorithm must jointly estimate both image and corrupting phase error. Unlike traditional autofocusing approaches the model error correction step then incorporates the estimated phase error into the model matrix making it more representative of the collection that produced the measured phase history data. In [27]–[29] the SAR/SAL autofocusing problem is reformatted for three different image reconstruction algorithms. Whereas, in [30], [31] the digital holography autofocusing problem is reformatted into a model error correction step where the corrupting atmospheric phase error is modeled in the aperture or at intermediate planes along the slant path.

In [23]–[26] model error correction algorithms to mitigate *spatially-variant phase errors* are developed and tested. In [23], [24] the model-based atmospheric phase correction (MBAPC) algorithm is developed to specifically mitigate atmospheric phase errors corrupting SAL phase history data. MBAPC is a parametric extension of the spatially-variant model error correction algorithms developed in [25], [26]. In [23], [24] the efficacy of the MBAPC algorithm is established across a wide-range of atmospheric turbulence strengths utilizing an atmospheric ray trace simulation and high-fidelity modeling and simulation software. A comparison of the reconstruction performance of MBAPC with the algorithms developed in [25]–[27] is quantified using well-established image quality and reference-based metrics. As a result of the analysis , MBAPC algorithm is determined to provide the best reconstruction performance in terms of the selected metrics across a wide-range of atmospheric strengths [24].

In this paper, we conduct statistical performance analysis of the MBAPC algorithm and validate it via Monte Carlo simulations. Specifically, we derive the Cramer-Rao Lower Bound (CRLB) for the estimate of the unknown atmospheric model parameter. We show that the MBAPC algorithm asymptotically attains the CRLB as it is the maximum-likelihood estimator (MLE). To test the derived analytical expression for the CRLB we implement a Monte Carlo simulation consisting of numerous independent realizations of randomized target, additive complex white Gaussian noise (CWGN), and model coefficient. We compare the mean-squared error (MSE) to the derived CRLB and show good agreement with theory.

The rest of this paper is organized as follows: In section II we summarize an atmospheric SAL collection model that incorporates the spatially-variant phase errors induced by turbulence, originally derived by the authors in [5]. In section III a discretized version of the atmospheric SAL collection model is introduced. Furthermore, we elaborate on how this model is used in a sparse image formation (SIF) algorithm [34]. In section IV we summarize the MBAPC algorithm implemented to estimate and remove atmospheric model errors for the SIF algorithm. In section V we derive the CRLB for the MBAPC estimation kernel under the assumption of additive CWGN. In section VI we describe the SAL simulation parameters defining the Monte Carlo simulations used to evaluate the performance of the MBAPC algorithm. Lastly, we provide concluding remarks on the statistical performance analysis of MBAPC algorithm in section VII.

II. SAL Atmospheric Collection Model

Phase history data is measured for each transmitted and received LFM waveform as the sensor platform traverses the synthetic aperture. Considering a single (m^{th}) point target in the scene at location $\bar{\mathbf{p}}_\mathbf{m}$, the phase history data measured from a mono-static sensor is defined as follows,

$$\tilde{y}(f_k, \tau_n; \bar{\mathbf{p}}_\mathbf{m}) = \tilde{x}(\bar{\mathbf{p}}_\mathbf{m}, \tau_n) \exp[-j\phi_{SAL}(f_k, \tau_n, \bar{\mathbf{p}}_\mathbf{m})]; \quad (1)$$

where f_k corresponds to the k^{th} frequency sample out of K, τ_n corresponds to the n^{th} slow-time (waveform) sample out of N_p, and ϕ_{SAL} is the SAL phase of the corresponding to point target in the scene [5], [34], [35]. Let $\Delta R(\bar{\mathbf{p}}_\mathbf{m}, \tau_n) = R_m(\tau_n) - R_0(\tau_n)$ be the differential range to the target at Cartesian coordinate $\bar{\mathbf{p}}_\mathbf{m} = [u_m, v_m, w_m]$ in the scene; where the distance between the sensor platform and target is R_m and the distance between the sensor platform and the reference scene center (motion compensation point) is denoted by R_0. We define the SAL phase as follows,

$$\phi_{SAL}(f_k, \tau_n, \bar{\mathbf{p}}_\mathbf{m}) = \frac{4\pi f_k}{c} \Delta R(\bar{\mathbf{p}}_\mathbf{m}, \tau_n) \quad (2)$$

The effects of two-way propagation through atmosphere manifest as a target-dependent, time-varying perturbation on scene reflectivity [5], [11]. We consider only the phase perturbation imparted by the atmosphere in this analysis. The atmospheric phase perturbation on a target in the scene is modeled as a phase error on the isotropic reflectivity of the target, as follows,

$$\tilde{x}(\bar{\mathbf{p}}_\mathbf{m}, \tau_n) = x(\bar{\mathbf{p}}_\mathbf{m}) \exp\left[j\varphi(\bar{\mathbf{p}}_\mathbf{m}; \tau_n)\right]. \quad (3)$$

The measured phase history at each collected pulse corresponds to the coherent integration of all the individual target phase histories defined in Equation 1,

$$\tilde{y}(f_k, \tau_n) = \sum_{m=1}^{M} \tilde{x}(\bar{\mathbf{p}}_\mathbf{m}, \tau_n) \exp[-j\phi_{SAL}(f_k, \tau_n, \bar{\mathbf{p}}_\mathbf{m})]; \quad (4)$$

where, M corresponds to the total number of targets in the illuminated region of interest.

III. Image Reconstruction Algorithm

Given the SAL atmospheric collection model we can formulate an SIF optimization problem, which we solve using the algorithm developed in [34]. The coherent integration of all targets in the scene in Equation 4, can be written using a set of linear equations where the vectorized scene reflectivity is denoted by $\bar{\mathbf{x}} \in \mathcal{C}^{M\times 1}$ and the vectorized measured phase history is denoted by $\tilde{\mathbf{y}} \in \mathcal{C}^{KN_p\times 1}$, and

$$\tilde{\mathbf{y}} = \tilde{\mathbf{A}}(\mathbf{\Phi})\bar{\mathbf{x}} + \bar{\varepsilon} \tag{5}$$

where $\bar{\varepsilon} \in \mathcal{C}^{KN_p\times 1}$ is the additive CWGN, such that, $\bar{\varepsilon} \sim \mathcal{CN}(\bar{\mathbf{0}}, \sigma_\varepsilon \mathbf{I})$. The SAL atmospheric collection model is encapsulated in the matrix, $\tilde{\mathbf{A}}(\mathbf{\Phi}) \in \mathcal{C}^{KN_p\times M}$, where the atmospheric model errors are represented with $\mathbf{\Phi} \in \mathcal{R}^{M\times N_p}$. The SAL collection model is perturbed by unknown atmospheric phase errors that vary spatially throughout the illuminated target area. We represent the illuminated region as a grid of points in the ground plane, which is built into the model matrix as follows,

$$\tilde{\mathbf{A}}(\mathbf{\Phi}) = \begin{bmatrix} \mathbf{A_1}\text{diag}\{\bar{\beta}_\mathbf{1}\} \\ \mathbf{A_2}\text{diag}\{\bar{\beta}_\mathbf{2}\} \\ \vdots \\ \mathbf{A_{N_p}}\text{diag}\{\bar{\beta}_\mathbf{N_p}\} \end{bmatrix}$$

where $[\bar{\beta}_\mathbf{n}]_m = \exp(j[\bar{\psi}_\mathbf{n}]_m)$ and $\bar{\psi}_\mathbf{n} = [\mathbf{\Phi}]_n \in \mathcal{R}^{M\times 1}$ is the n^{th} vectorized atmospheric phase error perturbation on the n^{th} waveform out of N_p collected across the synthetic aperture. The predetermined collection matrix, $\mathbf{A_n} \in \mathcal{C}^{K\times M}$, for the n^{th} waveform is defined based on the SAL phasor in Equation 4. We express the elements in $\mathbf{A_n}$ as follows,

$$[\mathbf{A_n}]_{k,m'} = \exp\left(-j\frac{4\pi f_k}{c}\Delta R(\bar{\mathbf{p}}_{\mathbf{m}'}, \tau_n)\right) \tag{6}$$

where the image reconstruction grid defined in the ground plane is represented by the $\bar{\mathbf{p}}_{\mathbf{m}'} = [u_{m'}, v_{m'}, 0]$. The density of points in the reconstruction grid (ν) is a free parameter in the reconstruction and with the correct prior information super-resolution reconstructions are possible.

In [25]–[27], [34] a sparse image formation algorithm is developed that enforces sparsity by introducing a ρ-norm prior on the least-squares estimation problem. Utilizing a $\rho = 1$ we write the image estimation step as follows,

$$\hat{\mathbf{x}}^{i+1} = \arg\min_{\bar{\mathbf{x}}} ||\tilde{\mathbf{y}} - \tilde{\mathbf{A}}(\mathbf{\Phi}^i)\bar{\mathbf{x}}^i||_2^2 + \lambda_1||\bar{\mathbf{x}}^i||_1; \tag{7}$$

where λ_1 is a Lagrangian multiplier that enforces sparsity in the estimated scene reflectivity. In [34] the Conjugate Gradient (C.G.) algorithm is used to iteratively solve for the optimal solution, $\hat{\mathbf{x}}^{i+1}$, which we reproduce here for the convenience of the readers,

$$C.G.\left\{\left(\tilde{\mathbf{A}}^H\tilde{\mathbf{A}} + \lambda_1 W_1(\hat{\mathbf{x}}^i)\right)\hat{\mathbf{x}}^{i+1} = \tilde{\mathbf{A}}^H\tilde{\mathbf{y}}\right\}. \tag{8}$$

Each image reconstruction step utilizes the most up to date model matrix, $\tilde{\mathbf{A}} = \tilde{\mathbf{A}}(\mathbf{\Phi}^i)$, and the previous estimate of the image, $\hat{\mathbf{x}}^i$. The sparsity constraint is encapsulated in $W_1(\hat{\mathbf{x}}^i)$, which is defined as follows for $\rho = 1$,

$$W_1(\hat{\mathbf{x}}) = \text{diag}\left[1/(|\hat{\mathbf{x}}|^2 + \epsilon)^{1/2}\right]; \tag{9}$$

where we set $\epsilon = 10E^{-5}$. Sparse image formation is performed efficiently using Conjugate Gradient, which is iteratively implemented until convergence is obtained [34]. Convergence of the algorithm is defined using the normalized error between current and previous estimates of the scene reflectivity, $\frac{||\hat{\mathbf{x}}^i - \hat{\mathbf{x}}^{i-1}||}{||\hat{\mathbf{x}}^{i-1}||} < \eta = 10E^{-3}$ [25]–[27].

IV. Model-based Atmospheric Phase Correction Algorithm

The previous sparse image formation algorithm will reconstruct an image using unperturbed and atmospherically perturbed phase history data. However, the algorithm has no way of mitigating the atmospheric phase errors corrupting phase history data. If the phase errors remain un-compensated the sparse image formation will reconstruct erroneous targets in locations corresponding to increased side-lobes as opposed to actual target locations [23]–[27]. The atmospheric phase errors must be estimated and incorporated in to the model matrix to reconstruct an image of the targets without side-lobes.

To estimate the atmospheric model errors we implement the MBAPC algorithm. The MBAPC algorithm parametrically represents atmospheric phase errors using a set of orthogonal spatial basis sets: Zernike polynomials and Fourier-series. We incorporate the spatial basis sets into the aforementioned perturbed scene reflectivity (Equation 3) at the n^{th} pulse as follows,

$$\tilde{\mathbf{x}}_\mathbf{n} = \mathbf{T}\bar{\beta}_\mathbf{n}. \tag{10}$$

We represent the element-wise multiplication between scene reflectivity and atmospheric phase error using a diagonalized reflectivity matrix, $\mathbf{T} = \text{diag}\{\bar{\mathbf{x}}\} \in \mathcal{C}^{M\times M}$. The atmospheric phasor is denoted on a per-pulse basis using, $\bar{\beta}_\mathbf{n} \in \mathcal{C}^{M\times 1}$. We denote the parameterized atmospheric phasor by making it a function of the unknown coefficients, $\bar{\beta}(\bar{\alpha}_\mathbf{n})$, where the atmospheric phase perturbation is modeled using a set of linear equations $\bar{\psi}_\mathbf{n} = \mathbf{Z}\bar{\alpha}_\mathbf{n}$; where, considering N_o coefficients, $\mathbf{Z} \in \mathcal{R}^{M\times N_o}$ represents the atmospheric basis set. The unknown coefficients that must be estimated are represented using $\bar{\alpha}_\mathbf{n} \in \mathcal{R}^{N_o\times 1}$ and are allowed to vary non-parametrically from waveform-to-waveform, n [23]–[27].

The n^{th} waveform's phase history data is discretized as the complex vector containing the K frequency samples and can be written as follows,

$$\tilde{\mathbf{y}}_\mathbf{n} = \mathbf{A_n}\mathbf{T}\bar{\beta}(\bar{\alpha}_\mathbf{n}) + \bar{\varepsilon}_\mathbf{n}. \tag{11}$$

Utilizing the measured phase history data, $\tilde{\mathbf{y}}_\mathbf{n} \in \mathcal{C}^{K\times 1}$, the expected model matrix, $\mathbf{A_n}$, and the current estimate of the scene reflectivity, $\hat{\mathbf{x}}^{i+1}$, we formulate the following nonlinear least squares estimation problem [24],

$$\hat{\alpha}_{\mathbf{n}}^{i+1} = \arg\min_{\bar{\alpha}_{\mathbf{n}}} ||\tilde{\mathbf{y}}_{\mathbf{n}} - \tilde{\mathbf{A}}_{\mathbf{n}}^{i}\mathbf{T}^{i+1}\bar{\beta}(\bar{\alpha}_{\mathbf{n}})||_2^2; \tag{12}$$

which utilizes the latest estimate of the scene reflectivity, $\mathbf{T}^{i+1}$, and the latest estimate of the model error, $\bar{\alpha}_{\mathbf{n}}^{i}$ built into the model matrix, $\tilde{\mathbf{A}}_{\mathbf{n}}^{i}$, using Equation 6.

The nonlinear least squares problem is equivalent to the maximum-likelihood estimator of the n^{th} waveform's coefficients assuming additive CWGN. At each iteration of model error estimation step we consider each of the N_p waveforms individually. Using the measured complex phase history data we iteratively search for the optimal combination of target reflectivity and atmospheric phase error in the least squares sense. Therefore, for the n^{th} waveform's phase history we fit the spatially-variant phase error (parameterized by atmospheric basis sets) that best perturbs the most recent estimate of the scene reflectivity using nonlinear least squares in Equation 12. The model errors estimated in this step account for any phase perturbations present in the phase history that are not in the current model matrix.

We solve the nonlinear least squares estimation using Conjugate Gradient guided by the analytical gradient, $\nabla\bar{\alpha}_{\mathbf{n}} \in \mathcal{R}^{N_o\times 1}$. Taking the first partial derivative of the nonlinear least squares cost function we arrive at the following analytical expression for the gradient [24],

$$\nabla\bar{\alpha}_{\mathbf{n}} = \frac{\partial}{\partial\bar{\alpha}_{\mathbf{n}}}||\tilde{\mathbf{y}}_{\mathbf{n}} - \mathbf{A}_{\mathbf{n}}\mathbf{T}\bar{\beta}(\bar{\alpha}_{\mathbf{n}})||_2^2 \tag{13}$$

$$= 2\mathrm{Im}\left\{\tilde{\mathbf{B}}_{\mathbf{n}}^{H}\left(\tilde{\mathbf{y}}_{\mathbf{n}} - \mathbf{A}_{\mathbf{n}}\mathbf{T}\bar{\beta}(\bar{\alpha}_{\mathbf{n}})\right)\right\} \tag{14}$$

$$= -j\tilde{\mathbf{B}}_{\mathbf{n}}^{H}\left(\tilde{\mathbf{y}}_{\mathbf{n}} - \mathbf{A}_{\mathbf{n}}\mathbf{T}\bar{\beta}(\bar{\alpha}_{\mathbf{n}})\right); \tag{15}$$

where $\tilde{\mathbf{B}}_{\mathbf{n}} = \mathbf{A}_{\mathbf{n}}\mathbf{T}\mathbf{\Lambda}(\bar{\alpha}_{\mathbf{n}})\mathbf{Z} \in \mathcal{C}^{K\times N_o}$ and $\mathbf{\Lambda}(\bar{\alpha}_{\mathbf{n}}) = \mathrm{diag}\{\bar{\beta}(\bar{\alpha}_{\mathbf{n}})\} \in \mathcal{C}^{M\times M}$. The result is reminiscent of similar gradients for IQM optimization [19]–[21], in that, the non-parameterized gradient is projected onto the orthonormal basis set, $\mathbf{Z}$. In section VII we provide the full derivation of the analytical gradient [24].

V. Cramer-Rao Lower Bound (CRLB)

Under the assumption of additive CWGN the maximum-likelihood estimate of the spatial coefficients, is given by the aforementioned nonlinear least-squares optimization. For an unbiased estimator the CRLB offers insight into the optimal estimation accuracy obtainable over a range of operating conditions i.e. signal-to-noise ratio (SNR). In this section we derive the CRLB for the unknown vector coefficient parameter, $\bar{\alpha}_{\mathbf{n}}$, assuming that both collection matrix, $\mathbf{A}_{\mathbf{n}}$, and the target, $\mathbf{T}$, are known. Assuming the regularity conditions hold, then the covariance matrix of an unbiased estimator for the unknown vector coefficients, $\hat{\alpha}_{\mathbf{n}}$, satisfies

$$\mathrm{cov}\{\hat{\alpha}_{\mathbf{n}}\} - \mathbf{F}^{-1} \geq \mathbf{0}; \tag{16}$$

which is interpreted as a positive semidefinite difference between the matrices [36]. Let $\ln[]$ be the natural logarithm, the Fisher information matrix entries are defined as follows,

$$[\mathbf{F}]_{o,o'} = -E\left[\frac{\partial^2}{\partial\alpha_{o'}\partial\alpha_o}\ln[p(\tilde{\mathbf{y}}_{\mathbf{n}};\bar{\alpha}_{\mathbf{n}})]\right] \tag{17}$$

and the expectation is taken with respect to $p(\tilde{\mathbf{y}}_{\mathbf{n}};\bar{\alpha}_{\mathbf{n}})$. Given this notation we denote the partial derivative with respect to a specific entry in the unknown coefficient vector, $\bar{\alpha}_{\mathbf{n}}$, as a scalar with the subscripts o and o', such that $\alpha_o = [\bar{\alpha}_{\mathbf{n}}]_o$.

The CRLB is a measure of the sharpness of the log-likelihood function which is quantified by taking the negative second derivative. Given that the log-likelihood function is a random variable, as it depends on the measured phase history data, we must take the expectation to arrive at the average sharpness of the log-likelihood function [36], [37]. In our case, $\tilde{\mathbf{y}}_{\mathbf{n}} \sim \mathcal{CN}(\mathbf{A}_{\mathbf{n}}\mathbf{T}\bar{\beta}(\bar{\alpha}_{\mathbf{n}}), \sigma_\varepsilon^2\mathbf{I})$. From which we can write the natural-logarithm of the posterior as follows,

$$\ln[p(\tilde{\mathbf{y}}_{\mathbf{n}};\bar{\alpha}_{\mathbf{n}})] = \ln[\det(2\pi\sigma_\varepsilon^2\mathbf{I})]^{1/2} - \ldots \frac{1}{\sigma_\varepsilon^2}||\tilde{\mathbf{y}}_{\mathbf{n}} - \mathbf{A}_{\mathbf{n}}\mathbf{T}\bar{\beta}(\bar{\alpha}_{\mathbf{n}})||_2^2. \tag{18}$$

Taking the first derivative of the log-likelihood with respect to the unknown, scalar parameter, α_o, yields a variance scaled version of the gradient,

$$\frac{2}{\sigma_\varepsilon^2}\mathrm{Re}\left\{j\left(\tilde{\mathbf{y}}_{\mathbf{n}}^{H} - \bar{\beta}(\alpha_n)^{H}\mathbf{T}^{H}\mathbf{A_n}^{H}\right)\mathbf{A}_{\mathbf{n}}\mathbf{T}\mathbf{\Lambda}(\bar{\alpha}_{\mathbf{n}})\bar{\mathbf{z}}_{\mathbf{o}}\right\}. \tag{19}$$

The analytical expression for the Fisher information is derived as follows,

$$[\mathbf{F}]_{o,o'} = \frac{2}{\sigma_\varepsilon^2}\begin{cases}\bar{\beta}(\bar{\alpha}_{\mathbf{n}})^{H}\mathbf{T}^{H}\mathbf{A_n}^{H}\mathbf{A}_{\mathbf{n}}\mathbf{T}\bar{\beta}(\bar{\alpha}_{\mathbf{n}}), & \text{if } o = o' \\ 0, & \text{otherwise}\end{cases}$$

This result comes from the underlying orthogonality of the spatial basis sets used in the MBAPC algorithm to model the spatially-variant nature of the atmospheric phase errors on each waveform. Under the assumption of orthogonality of the spatial basis set, the Fisher information matrix is a diagonal matrix with entries equal to the Fisher information for each respective entry in the unknown coefficient vector, $\bar{\alpha}_{\mathbf{n}} \in \mathcal{R}^{N_o\times 1}$,

$$\mathbf{F} = 2\left(\frac{\bar{\beta}(\bar{\alpha}_{\mathbf{n}})^{H}\mathbf{T}^{H}\mathbf{A_n}^{H}\mathbf{A}_{\mathbf{n}}\mathbf{T}\bar{\beta}(\bar{\alpha}_{\mathbf{n}})}{\sigma_\varepsilon^2}\right)\mathbf{I} \in \mathcal{R}^{N_o\times N_o}. \tag{20}$$

Inverting the Fisher information matrix produces the CRLB for the estimates of the unknown coefficient vector parameter,

$$\mathbf{F}^{-1} = \frac{1}{2}\left(\frac{\sigma_\varepsilon^2}{\bar{\beta}(\bar{\alpha}_{\mathbf{n}})^{H}\mathbf{T}^{H}\mathbf{A_n}^{H}\mathbf{A}_{\mathbf{n}}\mathbf{T}\bar{\beta}(\bar{\alpha}_{\mathbf{n}})}\right)\mathbf{I}. \tag{21}$$

Considering the diagonal elements of the covariance matrix we can write the CRLB for the estimate of a single coefficient from the MBAPC algorithm yielding,

$$\mathrm{var}[\alpha_o] \geq [\mathbf{F}^{-1}]_{o,o} = \frac{1}{2}\frac{\sigma_\varepsilon^2}{\bar{\beta}(\bar{\alpha}_{\mathbf{n}})^{H}\mathbf{T}^{H}\mathbf{A_n}^{H}\mathbf{A}_{\mathbf{n}}\mathbf{T}\bar{\beta}(\bar{\alpha}_{\mathbf{n}})}. \tag{22}$$

Thus the CRLB for the estimate of the unknown coefficient is derived in closed form providing an analytical method for quantifying the statistical performance of the MBAPC algorithm. The full derivation of the expectation of the second derivative of the log-likelihood to arrive at the Fisher information is provided in section VII.

VI. SAL Simulation

We design the SAL simulation to provide $K \times N_p$ phase history data from an illuminated region containing numerous randomly-distributed unit-amplitude point targets. The SAL sensor parameters used to simulate the phase history data are given in Table I. We assume a center wavelength of 1.55 μm which only requires 6.4 ms of collection time at a sensor platform velocity of 160 m/s to obtain the desired cross-range resolution. We critically sample the complex phase history data such that the unambiguous range and cross-range extent are matched to the diffraction limited spot size of the ladar in azimuth. In the simulations the randomly-distributed unit-amplitude point targets always fall within this circular region.

SAL Parameters	Value
Resolution, $\delta_a \delta_r$	$D_{\text{spot}}/32$
Center wavelength, λ_c	1.55μm
Number of pulses, N_p	32
Number of Frequency Samples, K	32
Collection Time, T_{synth}	6.4 ms
Platform Velocity, V_p	160 m/s
Platform Altitude, H_p	30 kft
Real Aperture Size, D_{ap}	6 inch
Diffraction Limited Spot Size, D_{spot}	$1.22\lambda_c R/D_{\text{ap}}$

TABLE I
SAL Simulation Parameters [24]

We perturb the ideal phase history data by randomly varying the first ten Zernike coefficients (ignoring constant term) across the synthetic aperture. An $i.i.d.$ random variation in the Zernike coefficients is different than a correlated atmospheric phase error. We use the random Zernike coefficients to test the model-based atmospheric phase correction algorithm's ability to estimate and remove a spatially-variant phase perturbation. The spatial perturbation applied is well-represented by the spatial basis set used in MBAPC. In other words, we apply a randomly varying Zernike perturbation in the ground plane and implement MBAPC using a Zernike basis set in the ground plane. In Figure 1[a-b] we plot the first and last waveform's spatially-variant phase error corrupting the target reflectivity. The coefficients are zero-mean, π-variance Gaussian random variables. Each coefficient is weighted according to Kolmogorov (power law) power spectral density, such that a majority of the power exists at the lower-order coefficients [6], [7], [32], as shown in Figure 1[c]. Lastly, in Figure 1[d] we plot the phase perturbation on each of the point targets in the scene, represented by the red dots in the spatially-variant phase, as a function of waveform.

Performing sparse reconstruction using the perturbed phase history data we note the drastic increase in cross-range side-lobes and the inherent loss of contrast. The spatially-variant phase errors correspond to errors in the phase history data that

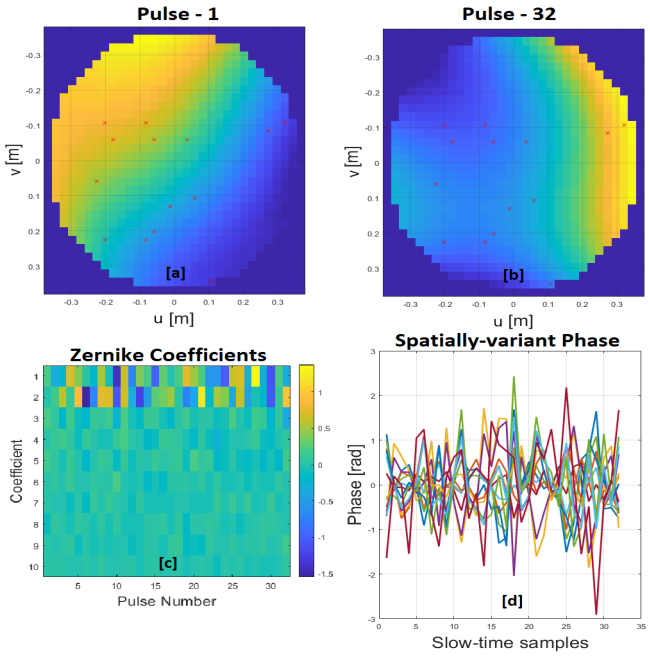

Fig. 1. [a-b] First and last waveform's spatially-variant phase error. [c] Realization of random Zernike coefficients with π-variance Normal distributions across the first 10 Zernike coefficients. The power in each coefficient decreases according to Kolmogorov PSD for D/r_0 of $1/4$. [d] A plot of each point target's random phase error resulting from the spatially-variant phase errors in [a-b].

are not captured in the model matrix. The sparse reconstruction algorithm treats the phase errors increase in side-lobes as a reflectivity that exists in the scene, as shown in Figure 2[b]. It can be seen that only after a model-error correction step is introduced the sparse reconstruction is able to separate phase error induced side-lobes from target reflectivities. In Figure 2[c-d] we show that utilizing the MBAPC algorithm the perturbed phase history reconstructs a high contrast image void of increased cross-range side-lobes..

A. Monte Carlo Results

In this section we focus on perturbing simulated SAL phase history data with a single Zernike coefficient. We select the first and third Zernike coefficient (Tip and Defocus) as defined by Noll [7], [38] and randomly vary the coefficient across the synthetic aperture. The random variation of the coefficient is a zero-mean, σ_α^2-variance Gaussian random variable. We implement a Monte Carlo simulation to test the MBAPC estimation accuracy by comparing the variance of the MBAPC estimates with the derived CRLB. Each realization of the Monte Carlo simulation instantiates a new realization of random Zernike coefficient which perturbs the simulated phase history according to Equation 11 and is corrupted by additive CWGN. We simulate numerous independent realizations of Zernike coefficient and additive CWGN over multiple SNR values (-20 dB to 20 dB).

The standard deviation of the additive noise is defined as follows,

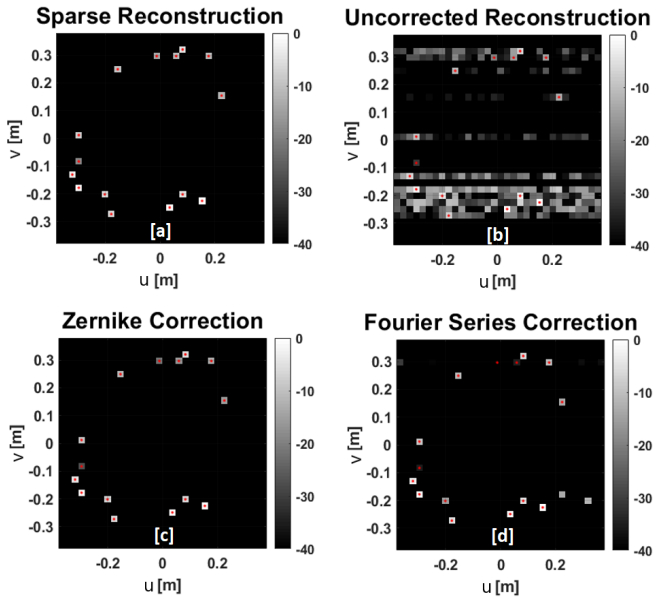

Fig. 2. Random realization using Figure 1 to generate spatially-variant phase error corrupting target reflectivity. [a] is ideal reconstructed reflectivity. [b] is reconstructed perturbed reflectivity without model error correction. [c] MBAPC Zernike correction. [d] MBAPC Fourier-series correction.

$$\sigma_\varepsilon = \sqrt{\frac{E[|\tilde{\mathbf{y}}|^2]}{10^{\text{SNR}}}} \tag{23}$$

such that we get an SNR defined in dB as follows,

$$\text{SNR}_{\text{dB}} = 10 \times \text{SNR} = 10\log_{10}\left(\frac{E[|\tilde{\mathbf{y}}|^2]}{\sigma_\varepsilon^2}\right). \tag{24}$$

Using the n^{th} waveform's collection model defined in Equation 11 we define the power as

$$E[|\tilde{\mathbf{y}}_\mathbf{n}|^2] = E[(\mathbf{A_n}\mathbf{T}\bar{\beta}(\bar{\alpha}_\mathbf{n}))^H \mathbf{A_n}\mathbf{T}\bar{\beta}(\bar{\alpha}_\mathbf{n})] \tag{25}$$

$$= \frac{\bar{\beta}(\bar{\alpha}_\mathbf{n})^H \mathbf{T}^H \mathbf{A_n}^H \mathbf{A_n}\mathbf{T}\bar{\beta}(\bar{\alpha}_\mathbf{n})}{K}. \tag{26}$$

Recall the CRLB derived contains a similar expression in the denominator. Utilizing the definition for average signal power, $E[|\tilde{\mathbf{y}}_\mathbf{n}|^2]$, we can write the CRLB in terms of SNR,

$$\text{var}[\alpha_o] \geq \frac{1}{2}\left(\frac{K}{K}\right)\frac{\sigma_\varepsilon^2}{\bar{\beta}(\bar{\alpha}_\mathbf{n})^H \mathbf{T}^H \mathbf{A_n}^H \mathbf{A_n}\mathbf{T}\bar{\beta}(\bar{\alpha}_\mathbf{n})} \tag{27}$$

$$\geq \left(\frac{1}{2K}\right)\frac{\sigma_\varepsilon^2}{E[|\tilde{\mathbf{y}}_\mathbf{n}|^2]} \tag{28}$$

$$\geq \left(\frac{1}{2K}\right)10^{-\text{SNR}}; \tag{29}$$

where K is the number of frequency samples in the n^{th} waveform's phase history data, $\tilde{\mathbf{y}}_\mathbf{n}$. Taking the $10\log_{10}$ of each side results in a CRLB in dB, as follows,

$$10\log_{10}(\text{var}[\alpha_o]) \geq 10\log_{10}\left(\left(\frac{1}{2K}\right)10^{-\text{SNR}}\right) \tag{30}$$

$$\geq -\text{SNR}_{\text{dB}} - 10\log_{10}(2K) \tag{31}$$

Using the parameters of the Monte Carlo simulation, $K = 32$ frequency samples the constant offset in the CRLB is $10\log_{10}(64) \approx 18$.

Each SAL realization simulated $N_p = 32$ waveforms, with each waveform having a random Zernike coefficient representing a spatially-variant phase error corrupting the underlying isotropic scene reflectivity. We assume that the scene, $\mathbf{T} = \text{diag}\{\bar{\mathbf{x}}\}$, is known for this analysis. Each of the independent SAL simulations contains a different random realization of sparse scene reflectivity, producing a unique random $\mathbf{T}$ for each independent realization in the Monte Carlo simulation. For the Monte Carlo results presented herein we fixed the probability that a unit-amplitude point target appears in the scene to $p = 0.05$ and we form a randomly-distributed scene of point targets using Matlab's in-built function *sprand* ($\bar{x} \sim \text{sprand}(p)$).

We plot a single realization of a randomly generated scene and Zernike coefficient in Figure 3. Along with the random realization of Zernike coefficient value we also plot the estimated coefficient value using MBAPC algorithm and the associated estimation error. In Figure 4 we plot the real and imaginary parts of a random realization of the Fourier-series coefficients used to test the MBAPC algorithm. Along with the applied coefficients, we plot the estimated real and imaginary parts as well as the associated estimation error. Randomly varying the location of the point targets in the scene removes any potential bias of the MBAPC algorithm to scene structure. The MBAPC fits a known spatial basis set to each waveform's phase history data. The point target locations provide the samples of the spatially-variant phase error that are used to fit the nonlinear least squares.

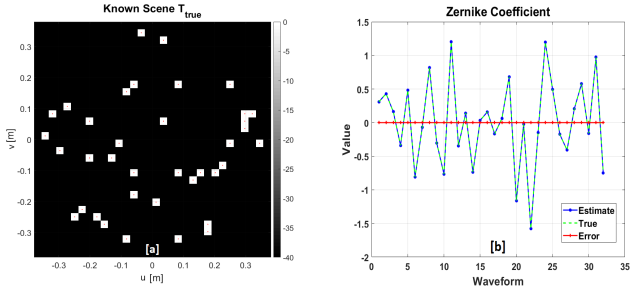

Fig. 3. [a] Random realization of the known, sparse scene reflectivity. [b] Random realization of Zernike coefficient (o = 1 - Tip) $\alpha_n \sim \mathcal{N}(0, \sigma_\alpha^2)$. The coefficient variance is set to $\sigma_\alpha^2 = 1/8$.

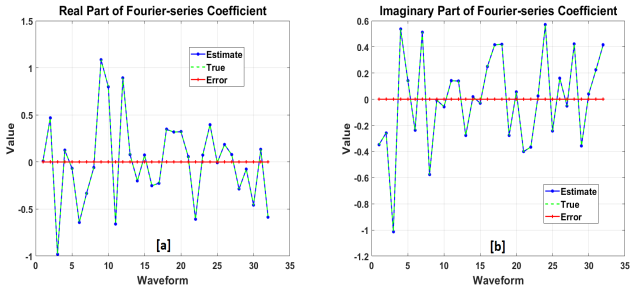

Fig. 4. Random realization of Fourier-series coefficient $\sim \mathcal{N}(0, \sigma_\alpha^2)$: [a] Real part and [b] Imaginary part. The coefficient variance is set to $\sigma_\alpha^2 = 1/8$.

A plot of the derived analytical expression for the CRLB and the MSE from the Monte Carlo simulation is shown in Figure 5. We found that the MBAPC algorithm converges to the correct estimate of the coefficient within a few iterations. However, we found that numerous iterations for the real Zernike and complex Fourier-series coefficient is needed for the algorithm to converge on the CRLB at SNRs higher than 20 dB.

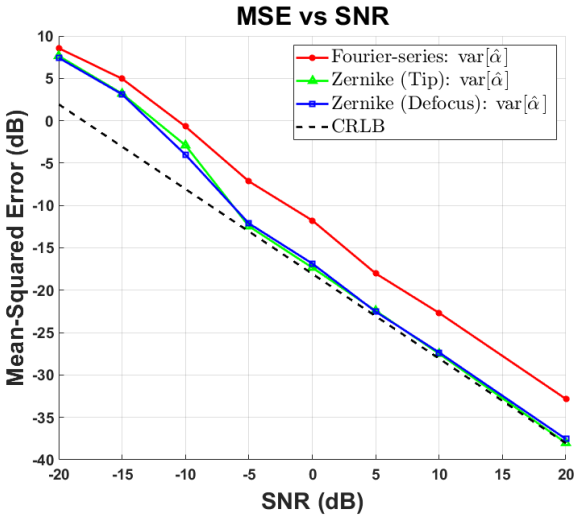

Fig. 5. MSE between true and estimated coefficient averaged over numerous independent realizations of random coefficients across multiple SNR levels. $K = 32$ and $10\log_{10}(64) \approx 18$. The coefficient variance is set to $\sigma_\alpha^2 = 1/8$.

Computing the MSE is straight-forward for the real-valued Zernike coefficients. However, for the complex-valued Fourier-series coefficients we compute the MSE using both real and imaginary parts stacked into a single array. Using this concatenated array of estimates and true values we compute the MSE. Both real and complex MSE show good agreement with the analytically derived CRLB expression. The MBAPC MSE attains the CRLB for the Zernike coefficients considered in this Monte Carlo. However, we note that there is an offset of nominally $10\log_{10}(\pi) \approx 5$ dB in the complex Fourier-series Monte Carlo results. The overall trend of the MSE follows that of the derived CRLB across all considered SNRs.

Further analyzing MBAPC algorithm we slightly tweak the aforementioned Monte Carlo simulation to produce $N_p N_{real} = 32 \times 50 = 1,600$ $i.i.d.$ realizations of the CWGN corrupted phase history data using a single perturbing Zernike coefficient. The value for the unknown coefficient parameter was selected randomly at the beginning of the simulation and held constant over all random realizations. Using this Monte Carlo simulation we investigate the bias associated with the MBAPC algorithm. In Figure 5, we demonstrated that the MBAPC algorithm asymptotically attains the CRLB, offering the best estimation accuracy attainable under the assumption of additive CWGN. In Figure 6, we plot the true parameter used at each SNR level and the associated distribution of estimates produced by the MBAPC algorithm at each respective SNR value. We arrive at the conclusion that MBAPC is unbiased by the fact that ensemble average of the numerous MBAPC estimates is the true parameter value. These results suggest that the MBAPC algorithm is the maximum-likelihood estimator of the unknown coefficient parameter, in that, MBAPC is asymptotically unbiased and attains the CRLB.

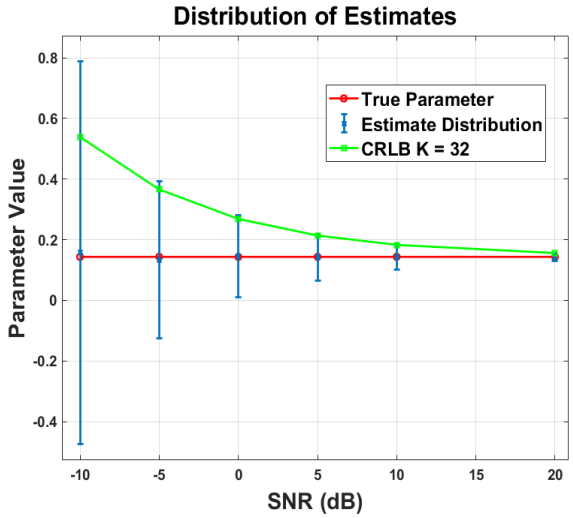

Fig. 6. Plot of the distribution of the MBAPC algorithm's estimates from the Monte Carlo simulation data with $K = 32$ frequency samples and $N_p N_{real} = 32 \times 50 = 1600$ $i.i.d.$ realizations of additive CWGN. The estimates correspond to the linear Zernike mode, Tip ($o = 1$).

The final Monte Carlo simulation we run in this section tests the MBAPC algorithm's ability to efficiently estimate multiple coefficient parameters. To do this we modify the Monte Carlo simulation to perturb phase history data with $N_o = 2$ Zernike modes. We utilize first two non-constant Zernike modes, commonly referred to as Tip and Tilt [6], [7], [38], corresponding to the orthogonal linear terms in $u_{m'}$ and $v_{m'}$ dimensions of the ground plane, respectively. In the Monte Carlo simulation the Zernike coefficients are $i.i.d.$ random variables, distributed according to $\sim \mathcal{N}(\bar{\mathbf{0}}, \sigma_\alpha^2 \mathbf{I})$. Similar to the previous Monte Carlo we generate $N_p N_{real} = 32 \times 50 = 1600$ $i.i.d.$ realizations of phase history data corrupted by additive CWGN. Using the MBAPC algorithm we simultaneously estimate both unknown coefficient parameters from phase history data corrupted by additive CWGN. The estimated coefficient vector, $\hat{\alpha}_{\mathbf{n}}$, is then compared with the applied coefficient vector, $\bar{\alpha}_{\mathbf{n}}$, to obtain the respective covariance matrix. In Figure 7 we plot the diagonal entries in the covariance matrix and compare the result to the derived analytical CRLB.

Similar to the previous Monte Carlo simulation results the computed MSE attains the derived CRLB for SNR $\geq$ -5 dB. In this region of reasonably high SNR (SNR $\geq$ -5 dB) we consistently find that the MBAPC algorithm is an efficient estimator of the unknown coefficient parameters. In regions where the measured signal is significantly buried in the additive CWGN, we note a significant deviation in the estimation accuracy of the MBAPC algorithm. For a nonlinear estimator this low SNR region is commonly referred to as the Threshold region [36]. As described in [36], the Threshold region results from having a likelihood function with side-lobes that are larger than the main-lobe centered about the true parameter value. In this region the MLE will consistently select the maximum value corresponding the the

side-lobe, which corresponds to a larger estimation error. Furthermore, as the number of independent realizations is increased the higher probability of larger estimation error will correspondingly increase the estimators variance, creating a larger divergence between derived CRLB and MLE variance. We classify the Threshold region operating condition for the MBAPC algorithm as any SNR $<$ -5 dB.

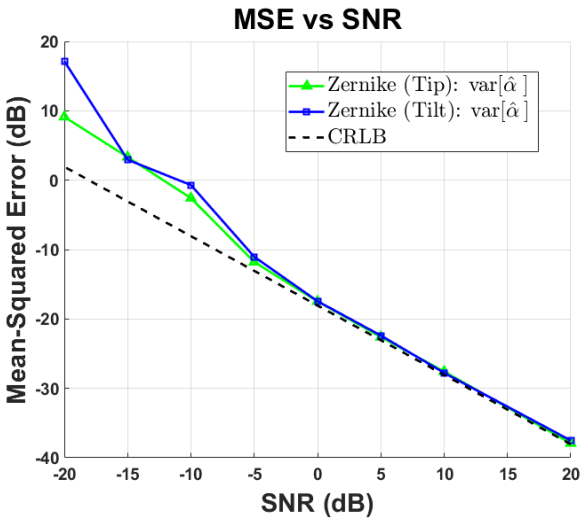

Fig. 7. MSE between true and estimated coefficients ($N_o = 2$) averaged over numerous independent realizations of random coefficients across multiple SNR levels. $K = 32$ and $10\log_{10}(64) \approx 18$.

B. Computational Complexity

The computational complexity of computing the cost function in Equation 12 is $\mathcal{O}(K(M+1)+N_oM)$. Similarly, the computational cost of computing the analytical gradient in Equation 14 is $\mathcal{O}((K+N_o)M+KN_o(M^2+1))$. Each iteration of the Conjugate Gradient algorithm utilizes the analytical gradient to arrive at the optimal value for the nonlinear least squares cost function. We arrive at these numbers assuming non-optimized matrix multiply complexity; where a $P \times Q$ matrix $\mathbf{G}$ multiplied by $Q \times R$ matrix $\mathbf{H}$ results in a $\mathcal{O}(PQR)$ computational complexity. A plot of the average computational time as a function of K and M for a fixed model order N_o is shown in Figure 8. Based on the plots, we conclude that the computational complexity of the cost function and gradient is linear with respect to number of frequencies, K, and quadratic with respect to number of points in the reconstruction grid, M. Furthermore, the gradient computation is the most computationally expensive aspect of the MBAPC algorithm. We tested the algorithm on an HP laptop with Intel(R) Core(TM) i5-6300U CPU at 2.40 GHz with 16 GB of RAM using 64 bit Windows 10 and MATLAB R2018b.

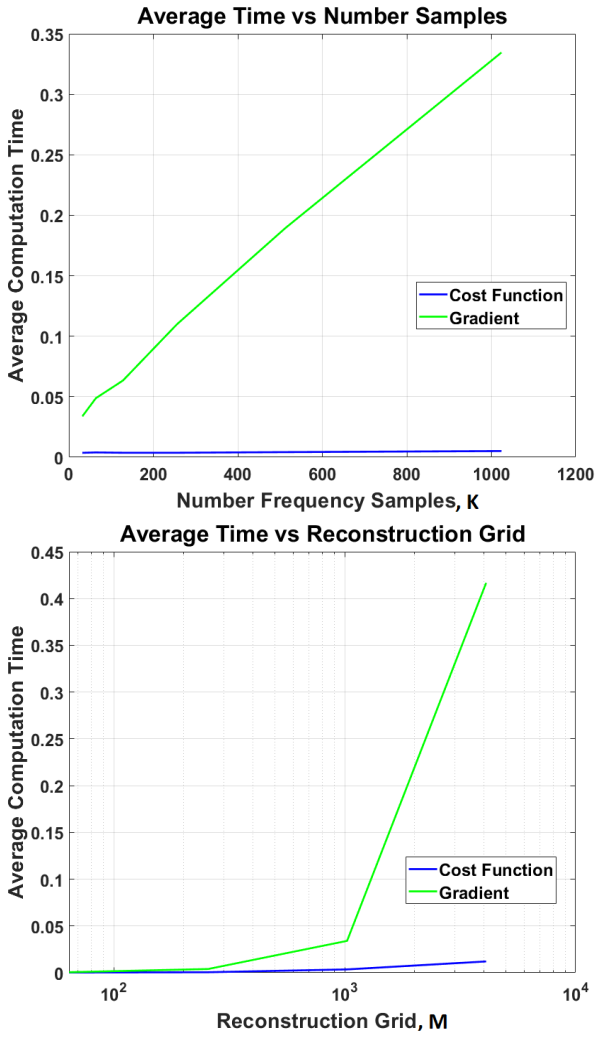

Fig. 8. Average time to compute MBAPC cost function and gradient as a function of K and M.

VII. Conclusion

In this paper we introduced an atmospheric SAL collection model used as the basis for the model-based atmospheric phase correction (MBAPC) algorithm. We summarized the MBAPC algorithm and derived the analytical gradient used to guide the algorithm to optimal estimate of the unknown model error. The MBAPC algorithm enables mitigation of atmospheric phase errors that would otherwise perturb the measured phase history data and corrupt reconstructed SAL imagery. MBAPC utilizes well-established spatial basis sets to model the atmospheric phase errors corrupting the underlying isotropic scene reflectivity. The algorithm introduces a nonlinear least squares estimation problem, that fits the spatial basis sets to the measured phase history data corrupted by the presence of additive CWGN. Under this assumption, the MBAPC algorithm produces the maximum-likelihood estimate of the spatial basis set coefficients. Utilizing the maximum-likelihood estimate for the coefficients, the collection matrix is updated enabling reconstruction of well-focused SAL imagery, effectively mitigating the detrimental effects of the spatially-variant atmospheric phase error as demonstrated in [23], [24] and throughout this paper.

In previous publications [23], [24], we derived the MBAPC algorithm and demonstrated its reconstruction efficacy over a wide-range of atmospheric turbulence strengths. It was shown that the MBAPC offered the best reconstruction performance in terms of image quality metrics when compared to other

candidate algorithms [25]–[27] across all considered turbulence strengths. The analysis presented in this paper expands upon previous research by formalizing the statistical efficacy of MBAPC algorithm as a function of SNR. In this paper, we conduct a statistical performance analysis and validate the results using a Monte Carlo simulation. Specifically, we derive an analytical expression for the Cramer-Rao Lower Bound (CRLB) for the estimate of the unknown vector parameters.

Based on the orthogonality property of the spatial basis sets implemented in MBAPC, we derived a general expression for the Fisher information matrix. For the case of orthogonal basis sets, we demonstrated that the Fisher information matrix is a diagonal matrix composed of each coefficient's respective Fisher information. We derived the closed-form expression of the CRLB for the unknown vector parameter by inverting the Fisher information matrix. We illustrated that statistical performance of the MBAPC algorithm depends primarily on the SNR and the number of measured frequency samples, K.

Utilizing the Monte Carlo simulation consisting of numerous independent realizations we show that the MBAPC algorithm estimates are unbiased and asymptotically attain the CRLB. We demonstrated good agreement between computed mean-squared error (MSE) and derived CRLB expression across a wide-range of signal-to-noise ratios for both Zernike and Fourier-series basis sets.Considering the first two Zernike polynomials in the multi-parameter case ($N_o = 2$), we demonstrated that MBAPC can simultaneously produce unbiased estimates of the unknown coefficients corresponding to multiple spatial modes. Furthermore, the variance of the multiple estimates asymptotically obtains the CRLB as number of $i.i.d.$ realizations grows. Therefore, we conclude by stating that the MBAPC algorithm is the maximum likelihood estimator for the unknown vector coefficients and is asymptotically efficient.

ACKNOWLEDGMENT

The views expressed in this document are those of the authors and do not reflect on the official policy of the Air Force, Department of Defense, or U.S. Government.

APPENDIX I: FIRST PARTIAL DERIVATIVE

Letting $\tilde{\mathbf{y}}_\mathbf{n} \in \mathcal{C}^{K\times 1}$ be the measured phase history for the n^{th} waveform, $\mathbf{A_n} \in \mathcal{C}^{K\times M}$ be the expected model matrix, and $\mathbf{T} \in \mathcal{C}^{M\times M}$ represent a diagonal matrix of scene reflectivities, the estimate of the phase history for the n^{th} pulse is defined as [24],

$$\hat{\mathbf{y}}_\mathbf{n} = \mathbf{A_n}\mathbf{T}\bar{\beta}(\bar{\alpha}_\mathbf{n}). \tag{32}$$

Expanding the quadratic equation,

$$\tilde{\mathbf{y}}_\mathbf{n}^H\tilde{\mathbf{y}}_\mathbf{n} - 2\text{Re}\{\tilde{\mathbf{y}}_\mathbf{n}^H\hat{\mathbf{y}}_\mathbf{n}\} + \hat{\mathbf{y}}_\mathbf{n}^H\hat{\mathbf{y}}_\mathbf{n}. \tag{33}$$

The first term in this expanded quadratic does not depend on the coefficient vector, therefore results in the zero vector. Letting $\bar{\beta}(\bar{\alpha}_\mathbf{n}) \in \mathcal{C}^{M\times 1}$, $\mathbf{Z} \in \mathcal{R}^{M\times N_o}$, $\bar{\alpha}_\mathbf{n} \in \mathcal{R}^{N_o\times 1}$, $\mathbf{\Lambda}(\bar{\alpha}_\mathbf{n}) = \text{diag}\{\bar{\beta}(\bar{\alpha}_\mathbf{n})\} \in \mathcal{C}^{M\times M}$, and $\bar{\xi}^H = \tilde{\mathbf{y}}_\mathbf{n}^H\mathbf{A_n}\mathbf{T} \in \mathcal{C}^{1\times M}$ we find the second term's gradient as follows [24],

$$\frac{\partial}{\partial\bar{\alpha}_\mathbf{n}}\bar{\xi}^H\bar{\beta}(\bar{\alpha}_\mathbf{n}) = \bar{\xi}^H\frac{\partial}{\partial\bar{\alpha}_\mathbf{n}}\bar{\beta}(\bar{\alpha}_\mathbf{n}) \tag{34}$$

$$= \bar{\xi}^H(j\mathbf{\Lambda}(\bar{\alpha}_\mathbf{n})\mathbf{Z}). \tag{35}$$

Using the chain rule of differentiation we show that

$$\frac{\partial}{\partial\bar{\alpha}_\mathbf{n}}\bar{\beta}(\bar{\alpha}_\mathbf{n}) = \frac{\partial}{\partial\bar{\varphi}_\mathbf{n}}\bar{\beta}(\bar{\varphi}_\mathbf{n})\frac{\partial}{\partial\bar{\alpha}_\mathbf{n}}j\mathbf{Z}\bar{\alpha}_\mathbf{n} \tag{36}$$

$$= j\mathbf{\Lambda}(\bar{\alpha}_\mathbf{n})\mathbf{Z}; \tag{37}$$

which yields a diagonal matrix for the exponential which encapsulates element-wise multiplication with the chain rule, $j\mathbf{Z}$. The derivative of the argument of the exponential is simply the spatial basis set used in the MBAPC algorithm, shown as follows [24],

$$\frac{\partial}{\partial\bar{\alpha}_\mathbf{n}}j\mathbf{Z}\bar{\alpha}_\mathbf{n} = j\mathbf{Z}. \tag{38}$$

The last term in Equation 33 is a quadratic function of the unknown coefficient vector. We find it convenient to group matrices that are not functions of the unknown coefficient vector. Letting $\mathbf{\Omega_n} = \mathbf{T}^H{\mathbf{A_n}}^H\mathbf{A_n}\mathbf{T} \in \mathcal{C}^{M\times M}$, we can write the gradient as follows [24],

$$\frac{\partial}{\partial\bar{\alpha}_\mathbf{n}}\bar{\beta}(\bar{\alpha}_\mathbf{n})^H\mathbf{\Omega_n}\bar{\beta}(\bar{\alpha}_\mathbf{n}) = 2\bar{\beta}(\bar{\alpha}_\mathbf{n})^H\mathbf{\Omega_n}\frac{\partial}{\partial\bar{\alpha}_\mathbf{n}}\bar{\beta}(\bar{\alpha}_\mathbf{n}); \tag{39}$$

where

$$2\bar{\beta}(\bar{\alpha}_\mathbf{n})^H\mathbf{\Omega_n} \tag{40}$$

is the gradient of the quadratic matrix equation. The second term results from the chain rule, which we know from the Equation 37. Substituting this result in Equation 39 we arrive at the following expression for the gradient of the quadratic term,

$$\frac{\partial}{\partial\bar{\alpha}_\mathbf{n}}\bar{\beta}(\bar{\alpha}_\mathbf{n})^H\mathbf{\Omega_n}\bar{\beta}(\bar{\alpha}_\mathbf{n}) = 2\bar{\beta}(\bar{\alpha}_\mathbf{n})^H\mathbf{\Omega_n}(j\mathbf{\Lambda}(\bar{\alpha}_\mathbf{n})\mathbf{Z}) \tag{41}$$

Bringing the constants out front and pulling the common matrix out to the right, we can simplify the combined result for the gradient as follows [24],

$$\frac{\partial\ell(\bar{\alpha}_\mathbf{n})}{\partial\bar{\alpha}_\mathbf{n}} = -2\text{Re}\{j(\bar{\xi}^H - \bar{\beta}(\bar{\alpha}_\mathbf{n})^H\mathbf{\Omega_n})(\mathbf{\Lambda}(\bar{\alpha}_\mathbf{n})\mathbf{Z})\}. \tag{42}$$

We substitute in the original definitions for $\bar{\xi}$ and $\mathbf{\Omega_n}$ then take the transpose of the result in Equation 42 to arrive at the final expression for the gradient used in the MBAPC algorithm, as follows,

$$\nabla\bar{\alpha}_\mathbf{n} = \frac{\partial}{\partial\bar{\alpha}_\mathbf{n}}||\tilde{\mathbf{y}}_\mathbf{n} - \mathbf{A_n}\mathbf{T}\bar{\beta}(\bar{\alpha}_\mathbf{n})||_2^2 \tag{43}$$

$$= 2\text{Im}\left\{\tilde{\mathbf{B}}_\mathbf{n}^H\left(\tilde{\mathbf{y}}_\mathbf{n} - \mathbf{A_n}\mathbf{T}\bar{\beta}(\bar{\alpha}_\mathbf{n})\right)\right\} \tag{44}$$

$$= -j\tilde{\mathbf{B}}_\mathbf{n}^H\left(\tilde{\mathbf{y}}_\mathbf{n} - \mathbf{A_n}\mathbf{T}\bar{\beta}(\bar{\alpha}_\mathbf{n})\right); \tag{45}$$

where $\tilde{\mathbf{B}}_\mathbf{n} = \mathbf{A_n T \Lambda}(\bar{\alpha}_\mathbf{n})\mathbf{Z} \in \mathcal{C}^{K\times N_o}$ [24]. For a real coefficient vector (Zernike) we take the real part of the complex gradient, which reduces to the imaginary part as follows,

$$\text{Re}\{j(c_R + jc_I)\} = \text{Re}\{jc_R - c_I\} = -\text{Im}\{c_R + jc_I\}. \quad (46)$$

Appendix II: Second Partial Derivative

To arrive at an analytical expression for the CRLB, we need to solve for the partial derivative of the gradient with respect to the unknown parameter $\bar{\alpha}_\mathbf{n} \in \mathcal{R}^{N_o\times 1}$. We approach this derivation by first assuming, without loss of generality, that the first partial derivative is taken with respect to the o^{th} coefficient. The second partial derivative is then computed with respect to the o'^{th} coefficient, as follows,

$$\frac{\partial^2}{\partial\alpha_{o'}\partial\alpha_o}\log[p(\tilde{\mathbf{y}}_\mathbf{n};\bar{\alpha}_\mathbf{n})] = -\frac{1}{\sigma_\varepsilon^2}\frac{\partial}{\partial\alpha_{o'}}[\nabla\bar{\alpha}_\mathbf{n}]_o \quad (47)$$

We write the second partial derivative as follows,

$$\frac{2}{\sigma_\varepsilon^2}\text{Re}\left\{j\frac{\partial}{\partial\alpha_{o'}}\left(\tilde{\mathbf{y}}_\mathbf{n}^H\mathbf{A_n T} - \bar{\beta}(\bar{\alpha}_\mathbf{n})^H\mathbf{\Omega_n}\right)\mathbf{\Lambda}(\bar{\alpha}_\mathbf{n})\bar{\mathbf{z}}_\mathbf{o}\right\} \quad (48)$$

where $\bar{\mathbf{z}}_\mathbf{o} \in \mathcal{R}^{M\times 1}$ is the spatial basis set corresponding to the coefficient in the first partial derivative, α_o.

The gradient of the first term with respect to the second coefficient, $\alpha_{o'}$, is shown below,

$$\frac{\partial}{\partial\alpha_{o'}}\tilde{\mathbf{y}}_\mathbf{n}^H\mathbf{A_n T}\mathbf{\Lambda}(\bar{\alpha}_\mathbf{n})\bar{\mathbf{z}}_\mathbf{o} = \tilde{\mathbf{y}}_\mathbf{n}^H\mathbf{A_n T}\frac{\partial}{\partial\alpha_{o'}}\mathbf{\Lambda}(\bar{\alpha}_\mathbf{n})\bar{\mathbf{z}}_\mathbf{o} \quad (49)$$

Given that only $\mathbf{\Lambda}(\bar{\alpha}_\mathbf{n})$ is a function of the unknown parameter $\alpha_{o'}$, we compute the gradient as follows,

$$\frac{\partial}{\partial\alpha_{o'}}\mathbf{\Lambda}(\bar{\alpha}_\mathbf{n}) = \frac{\partial}{\partial\alpha_{o'}}\text{diag}\{\bar{\beta}(\bar{\alpha}_\mathbf{n})\} \quad (50)$$

$$= \text{diag}\{j\mathbf{\Lambda}(\bar{\alpha}_\mathbf{n})\bar{\mathbf{z}}_{\mathbf{o}'}\}; \quad (51)$$

which utilizes the previous result in Equation 37 and the fact that the partial derivative operates on each element of the matrix.

The gradient of the second term derived using the product rule of differentiation,

$$\frac{\partial}{\partial\alpha_{o'}}\bar{\beta}(\bar{\alpha}_\mathbf{n})^H\mathbf{\Omega_n}\mathbf{\Lambda}(\bar{\alpha}_\mathbf{n})\bar{\mathbf{z}}_\mathbf{o} = \frac{\partial}{\partial\alpha_{o'}}\bar{\beta}(\bar{\alpha}_\mathbf{n})^H\mathbf{\Omega_n}\mathbf{\Lambda}(\bar{\alpha}_\mathbf{n})\bar{\mathbf{z}}_\mathbf{o}\ldots$$
$$+\bar{\beta}(\bar{\alpha}_\mathbf{n})^H\mathbf{\Omega_n}\frac{\partial}{\partial\alpha_{o'}}\mathbf{\Lambda}(\bar{\alpha}_\mathbf{n})\bar{\mathbf{z}}_\mathbf{o} \quad (52)$$

Utilizing the previous result in Equation 37 and Equation 51 we can simply substitute them into Equation 52 and simplify,

$$-j\bar{\mathbf{z}}_{\mathbf{o}'}^T\mathbf{\Lambda}(\bar{\alpha}_\mathbf{n})^H\mathbf{\Omega_n}\mathbf{\Lambda}(\bar{\alpha}_\mathbf{n})\bar{\mathbf{z}}_\mathbf{o} + \ldots$$
$$j\bar{\beta}(\bar{\alpha}_\mathbf{n})^H\mathbf{\Omega_n}\left(\text{diag}\{\mathbf{\Lambda}(\bar{\alpha}_\mathbf{n})\bar{\mathbf{z}}_{\mathbf{o}'}\}\right)\bar{\mathbf{z}}_\mathbf{o}. \quad (53)$$

Substitution of the two parts back into Equation 48 we arrive at the final equation for the second partial derivative,

$$-\frac{2}{\sigma_\varepsilon^2}j\Big(-j\tilde{\mathbf{y}}_\mathbf{n}^H\mathbf{A_n T}\text{diag}\{\mathbf{\Lambda}(\bar{\alpha}_\mathbf{n})\bar{\mathbf{z}}_{\mathbf{o}'}\}\bar{\mathbf{z}}_\mathbf{o}\ldots$$
$$-j\bar{\mathbf{z}}_{\mathbf{o}'}^T\mathbf{\Lambda}(\bar{\alpha}_\mathbf{n})^H\mathbf{\Omega_n}\mathbf{\Lambda}(\bar{\alpha}_\mathbf{n})\bar{\mathbf{z}}_\mathbf{o}\ldots$$
$$+j\bar{\beta}(\bar{\alpha}_\mathbf{n})^H\mathbf{\Omega_n}\text{diag}\{\mathbf{\Lambda}(\bar{\alpha}_\mathbf{n})\bar{\mathbf{z}}_{\mathbf{o}'}\}\bar{\mathbf{z}}_\mathbf{o}\Big). \quad (54)$$

We bring the complex number $j = \sqrt{-1}$ out of the parenthesis, as it is common to all the terms, which changes the sign out front of the expression. The expectation of the second partial with respect to the posterior distribution, $\tilde{\mathbf{y}}_\mathbf{n} \sim \mathcal{CN}(\mathbf{A_n T}\bar{\beta}(\bar{\alpha}_\mathbf{n}), \sigma_\varepsilon^2\mathbf{I})$, yields the Fisher information, $\mathbf{F}_{o,o'}$. This result reduces to the following expression,

$$-\frac{2}{\sigma_\varepsilon^2}\Big(-\bar{\mathbf{z}}_{\mathbf{o}'}^T\mathbf{\Lambda}(\bar{\alpha}_\mathbf{n})^H\mathbf{\Omega_n}\mathbf{\Lambda}(\bar{\alpha}_\mathbf{n})\bar{\mathbf{z}}_\mathbf{o}\ldots$$
$$+\bar{\beta}(\bar{\alpha}_\mathbf{n})^H\mathbf{\Omega_n}\text{diag}\{\mathbf{\Lambda}(\bar{\alpha}_\mathbf{n})\bar{\mathbf{z}}_{\mathbf{o}'}\}\bar{\mathbf{z}}_\mathbf{o}\ldots$$
$$-\bar{\beta}(\bar{\alpha}_\mathbf{n})^H\mathbf{\Omega_n}\text{diag}\{\mathbf{\Lambda}(\bar{\alpha}_\mathbf{n})\bar{\mathbf{z}}_{\mathbf{o}'}\}\bar{\mathbf{z}}_\mathbf{o}\Big), \quad (55)$$

where the two like terms cancel to produce the entry into the Fisher information matrix,

$$[\mathbf{F}]_{o,o'} = 2\frac{\bar{\mathbf{z}}_{\mathbf{o}'}^T\mathbf{\Lambda}(\bar{\alpha}_\mathbf{n})^H\mathbf{\Omega_n}\mathbf{\Lambda}(\bar{\alpha}_\mathbf{n})\bar{\mathbf{z}}_\mathbf{o}}{\sigma_\varepsilon^2}. \quad (56)$$

This expression is an orthonormal basis set weighted version of the signal power, that is nonzero only when $o = o'$. Hence all off-diagonal entries in the Fisher information matrix are zero, resulting in the following compact expression for the Fisher information matrix,

$$\mathbf{F} = \frac{2}{\sigma_\varepsilon^2}\text{diag}\left\{\begin{bmatrix}\bar{\mathbf{z}}_\mathbf{1}^T\mathbf{\Lambda}(\bar{\alpha}_\mathbf{n})^H\mathbf{\Omega_n}\mathbf{\Lambda}(\bar{\alpha}_\mathbf{n})\bar{\mathbf{z}}_\mathbf{1}\\ \bar{\mathbf{z}}_\mathbf{2}^T\mathbf{\Lambda}(\bar{\alpha}_\mathbf{n})^H\mathbf{\Omega_n}\mathbf{\Lambda}(\bar{\alpha}_\mathbf{n})\bar{\mathbf{z}}_\mathbf{2}\\ \vdots\\ \bar{\mathbf{z}}_{\mathbf{N_o}}^T\mathbf{\Lambda}(\bar{\alpha}_\mathbf{n})^H\mathbf{\Omega_n}\mathbf{\Lambda}(\bar{\alpha}_\mathbf{n})\bar{\mathbf{z}}_{\mathbf{N_o}}\end{bmatrix}\right\}, \quad (57)$$

$\forall\ o \in [1,\ldots,N_o]$ where $\bar{\alpha}_\mathbf{n} \in \mathcal{R}^{N_o\times 1}$.

Further simplification of the Fisher information can be interpreted by considering how an orthonormal basis set modifies the ℓ_2-norm of the vector [39], [40],

$$||\mathbf{A_n T}\mathbf{\Lambda}(\bar{\alpha}_\mathbf{n})\bar{\mathbf{z}}_\mathbf{o}||_2^2 \leq ||\mathbf{A_n T}\bar{\beta}(\bar{\alpha}_\mathbf{n})||_2^2||\bar{\mathbf{z}}_\mathbf{o}||_2^2. \quad (58)$$

Substituting in the definition of $\mathbf{\Omega_n}$ the final result for the Fisher information is

$$\mathbf{F} = 2\left(\frac{\bar{\beta}(\bar{\alpha}_\mathbf{n})^H\mathbf{T}^H\mathbf{A_n}^H\mathbf{A_n T}\bar{\beta}(\bar{\alpha}_\mathbf{n})}{\sigma_\varepsilon^2}\right)\mathbf{I} \in \mathcal{R}^{N_o\times N_o}; \quad (59)$$

where $\mathbf{I} \in \mathcal{R}^{N_o\times N_o}$ is an $N_o \times N_o$ identity matrix.

Assuming equality in Equation 58 we obtain a Fisher information similar to that derived in [36] for the unknown phase of a complex sinusoid. In this case, we show that the diagonal elements correspond to the signal-to-noise ratio, which is also the case for estimating unknown phase of a complex sinusoid when the frequency is known [36], [37].

For the case where equality does not hold, Equation 59 will only approximate the Fisher information and result in a looser bound on the variance of the MBAPC estimate.

APPENDIX III: SPATIAL BASIS SETS

A. Zernike Polynomials

Decomposing the n^{th} pulse's atmospheric phase perturbation onto Zernike polynomials is done using Equation 10. Let O_L represent the lower order and O_U represent the upper order such that the total model order is $N_o = O_U - O_L$. Zernike polynomials are defined as follows when $\mu \neq 0$ [38],

$$z_o \text{ even}\left(\frac{\rho}{L}, \theta\right) = \sqrt{\upsilon + 1}\Psi_\upsilon^\mu\left(\frac{\rho}{L}\right)\sqrt{2}\cos(\mu\theta) \tag{60}$$

$$z_o \text{ odd}\left(\frac{\rho}{L}, \theta\right) = \sqrt{\upsilon + 1}\Psi_\upsilon^\mu\left(\frac{\rho}{L}\right)\sqrt{2}\sin(\mu\theta) \tag{61}$$

and when $\mu = 0$

$$z_o\left(\frac{\rho}{L}, \theta\right) = \sqrt{\upsilon + 1}\Psi_\upsilon^0\left(\frac{\rho}{L}\right); \tag{62}$$

where ρ is the radial distance, $L = D_{\text{spot}}$ is the radius of the circle, υ is the radial-order for the Zernike polynomial, μ is the azimuthal-order for the Zernike Polynomial, and $o = f(\mu, \upsilon)$ as defined by Noll in [38]. The radial polynomial is based on the well-known Jacobi polynomials,

$$\Psi_\upsilon^\mu\left(\frac{\rho}{L}\right) = \sum_{s=0}^{(\upsilon-\mu)/2} \frac{(-1)^s(\upsilon - s)!}{s![\frac{\upsilon+\mu}{2} - s]![\frac{\upsilon-\mu}{2} - s]!}\left(\frac{\rho}{L}\right)^{\upsilon-2s}$$

We vectorize the Zernike polynomials spatially and stack it into a basis set matrix, as follows,

$$\mathbf{Z} = \left[\bar{\mathbf{z}}_{\mathbf{O_L}}, \ldots, \bar{\mathbf{z}}_{\mathbf{O_U}}\right]. \tag{63}$$

A list of Zernike orders and how they relate to the azimuthal and radial orders is provided in Table II. The Piston mode (common spatial phase error) is not used in this analysis as all of the atmospheric perturbations vary spatially. The Zernike polynomial MATLAB code used to plot the Zernike modes and implement the basis sets in the MBAPC algorithm is available online through MATLAB Central File Exchange [41].

o	υ	μ		Classical Name
0	0	0		Piston
1	1	1	even	Tip
2	1	-1	odd	Tilt
3	2	0		Defocus

TABLE II
FIRST FOUR ZERNIKE POLYNOMIALS $\bar{\mathbf{z}}_\mathbf{o}$ [7], [38].

B. Fourier-series

Similar to Zernike polynomials, Fourier-series basis set is well-established in the atmospheric optics community as a high-fidelity phase screen modeling basis set [7], [33]. We adopt the definition of Fourier series used to simulate atmospheric phase screens in [33], which is repeated for the convenience of the reader as follows,

$$[\bar{\mathbf{z}}_{\mathbf{q},\mathbf{q}'}]_m = \exp\left[j2\pi\left(\frac{q[\bar{\mathbf{u}}]_m}{L} + \frac{q'[\bar{\mathbf{v}}]_m}{L}\right)\right], \tag{64}$$

where $\bar{\mathbf{u}} \in \mathcal{R}^{M\times 1}$ and $\bar{\mathbf{v}} \in \mathcal{R}^{M\times 1}$ are vectorized mesh-grids corresponding to the SAL image plane of diameter L. We arrive at a complex basis matrix by stacking Fourier series modes into a matrix,

$$\mathbf{Z} = \left[\bar{\mathbf{z}}_{-(\mathbf{N_c}-\mathbf{1}),-(\mathbf{N_c}-\mathbf{1})}, \ldots, \bar{\mathbf{z}}_{\mathbf{N_c}-\mathbf{1},\mathbf{N_c}-\mathbf{1}}\right]. \tag{65}$$

Using this complex basis set we estimate a complex coefficient using the MBAPC algorithm with the complex gradient in Equation 45. Recall that the model error correction assumes that the isotropic reflectivity is perturbed by a structured atmospheric phase error during the n^{th} waveform as follows

$$\tilde{\mathbf{x}}_\mathbf{n} = \mathbf{T}\bar{\beta}(\bar{\alpha}_\mathbf{n}). \tag{66}$$

Unlike the aforementioned Zernike basis set, $\mathbf{Z} \in \mathcal{C}^{M\times N_o}$ and $\bar{\alpha}_\mathbf{n} \in \mathcal{C}^{N_o\times 1}$ are both complex valued. The number of Fourier series modes is defined as $N_o = (2N_c - 1)^2 - 1$, ignoring the constant term that corresponds to a spatially-invariant phase error. The real part of the Fourier-series is kept as the atmospheric phase perturbation for the n^{th} waveform, $\bar{\varphi}_\mathbf{n} = \text{Re}\{\mathbf{Z}\bar{\alpha}_\mathbf{n}\}$; such that

$$[\bar{\beta}(\bar{\alpha}_\mathbf{n})]_m = \exp(j[\bar{\varphi}_\mathbf{n}]_m) = \exp(j[\text{Re}\{\mathbf{Z}\bar{\alpha}_\mathbf{n}\}]_m), \tag{67}$$

for all the M points considered in the reconstruction grid.

REFERENCES

[1] A. J. Stokes, M. P. Dierking, and D. J. Rabb. "Interferometric synthetic aperture ladar using code division multiple access apertures," *Appl. Opt.*, vol. 56, no. 17, pp. 5003–5012, Jun 2017.

[2] R. M. Neuroth, B. D. Rigling, E. G. Zelnio, E. A. Watson,V. J. Velten, and T. V. Rovito. "Asymptotic modeling of synthetic aperture ladar sensor phenomenology," *Proc. SPIE*, vol. 9475, pp. 94750D-1 - 94750D-6, 2015.

[3] B.W. Krause, J. Buck, C. Ryan, D. Hwang, P. Kondratko, A. Malm, A. Gleason, and S. Ashby. "Synthetic aperture ladar flight demonstration," *Lasers and Electro-Optics (CLEO), 2011 Conference on*, pp. 1–2, May 2011.

[4] C. Pellizzari, M. Spencer, N. Steinhoff, J. Belsher, G. Tyler, S. Williams, and S. Williams. "Inverse synthetic aperture ladar: a high-fidelity modeling and simulation tool," *Proc. SPIE*, vol. 8877, pp. 88770B–88770B–14, 2013.

[5] T. J. Karr. "Resolution of synthetic-aperture imaging through turbulence," *J. Opt. Soc. Am. A*, vol. 20, no. 6, pp. 1067–1083, Jun 2003.

[6] J. D. Schmidt. *Numerical Simulation of Optical Wave Propagation with Examples in MATLAB*. SPIE Washington, 2010.

[7] M. C. Roggeman and B. M. Welsh. *Imaging Through Turbulence*. New York: CRC Press., 1996.

[8] C. V. Jakowatz, D. E. Wahl, P. H. Eichel, D. C. Ghiglia, and P. A. Thompson. *Spotlight-Mode Synthetic Aperture Radar: A Signal Processing Approach*. Norwell, MA: Kluwer Academic Publishers, 1996.

[9] R. S. Goodman, W. G. Carrara, R. M. Majewski. *Spotlight Synthetic Aperture Radar - Signal Processing Algorithms*. Norwood, MA: Artech House, 1995.

[10] B. D. Rigling. "Multistage entropy minimization for sar image autofocus," *Proc. SPIE*, vol. 6237, pp. 62370J–62370J–10, 2006.

[11] R. M. Rustowicz, L. J. Barnes, B. L. Keaffaber, B. D. Rigling, J. W. Ross, and E. A. Watson. "Atmospheric effects and impact on target classification for synthetic aperture ladar (SAL) imagery," *Proc. SPIE*, vol. 10636, pp. 10636 - 10636 - 11, 2018.

[12] B. E. Schumm and M. P. Dierking. "Wave optics simulations of synthetic aperture ladar performance through turbulence," *J. Opt. Soc. Am. A*, vol. 34, no. 10, pp. 1888–1895, Oct 2017.

[13] C. V. Jakowatz Jr. and D. E. Wahl. "Eigenvector method for maximum-likelihood estimation of phase errors in synthetic-aperture-radar imagery," *J. Opt. Soc. Am. A*, vol. 10, no. 12, pp. 2539–2546, Dec 1993.

[14] D. E. Wahl, P. H. Eichel, D. C. Ghiglia, and C. V. Jakowatz Jr. "Phase gradient autofocus-a robust tool for high resolution sar phase correction," *IEEE Transactions on Aerospace and Electronic Systems*, vol. 30, no. 3, pp. 827–835, Jul 1994.

[15] Z. W. Barber and J. R. Dahl. "Synthetic aperture ladar imaging demonstrations and information at very low return levels," *Appl. Opt.*, vol. 53, no. 24, pp. 5531–5537, Aug 2014.

[16] S. Crouch and Z. W. Barber. "Laboratory demonstrations of interferometric and spotlight synthetic aperture ladar techniques," *Opt. Express*, vol. 20, no. 22, pp. 24237–24246, Oct 2012.

[17] J. R. Dahl and Z. W. Barber. "Sensitivity in synthetic aperture ladar imaging," *CLEO: 2014*, pp. SM4E.6, 2014.

[18] C. J. Pellizzari, J. Bos, M. F. Spencer, S. Williams, S. E. Williams, B. Calef, and D.C. Senft. "Performance characterization of phase gradient autofocus for inverse synthetic aperture ladar," *2014 IEEE Aerospace Conference*, pp. 1–11, March 2014.

[19] J. R. Fienup. "Synthetic-aperture radar autofocus by maximizing sharpness," *Opt. Lett.*, vol. 25, no. 4, pp. 221–223, Feb 2000.

[20] J. R. Fienup and J. J. Miller. "Aberration correction by maximizing generalized sharpness metrics," *J. Opt. Soc. Am. A*, vol. 20, no. 4, pp. 609–620, Apr 2003.

[21] J. R. Fienup and J.J. Miller. "Generalized image sharpness metrics for correcting phase errors," *Signal Recovery and Synthesis*, pp. STuD1, 2001.

[22] J. Kolman. Pace: an autofocus algorithm for sar. *Radar Conference, 2005 IEEE International*, pages 310–314, May 2005.

[23] R. S. Depoy Jr. and A. K. Shaw. "Mitigating atmospheric phase-errors in sal data using model-based reconstruction," *2019 IEEE National Aerospace and Electronics Conference (NAECON)*, pp. 384–390, 2019.

[24] R. S. Depoy Jr. and A. K. Shaw. "Algorithm to overcome atmospheric phase errors in sal data," *Appl. Opt.*, vol. 59, no. 1, pp. 140–150, Jan 2020.

[25] O. N. Onhon and M. Cetin. "Sar moving target imaging in a sparsity-driven framework," *Proc. SPIE*, vol. 8138, pp. 813806–813806–9, 2011.

[26] O. N. Onhon and M. Cetin. "Sparsity-driven image formation and space-variant focusing for sar," *18th IEEE International Conference on Image Processing (ICIP)*, pp. 173–176, Sept 2011.

[27] O. N. Onhon and M. Cetin. "A sparsity-driven approach for joint sar imaging and phase error correction," *IEEE Transactions on Image Processing*, vol. 21, no. 4, pp. 2075–2088, April 2012.

[28] T. Scarnati and T. Sanders. "Combination of correlated phase error correction and sparsity models for sar," *Proc. SPIE*, vol. 10222, pp. 10222 - 10222 - 11, 2017.

[29] C. J. Pellizzari, R. Trahan, H. Zhou, S. Williams, S. E. Williams, B. Nemati, M. Shao, and C. A. Bouman. "Synthetic aperature ladar: A model-based approach," *IEEE Transactions on Computational Imaging*, vol. 3, no. 4, pp. 901–916, Dec 2017.

[30] C. J. Pellizzari, M. F. Spencer, and C. A. Bouman. "Phase-error estimation and image reconstruction from digital-holography data using a bayesian framework," *J. Opt. Soc. Am. A*, vol. 34, no. 9, pp. 1659–1669, Sep 2017.

[31] C. J. Pellizzari, M. F. Spencer, and C. A. Bouman, "Imaging through distributed-volume aberrations using single-shot digital holography," *J. Opt. Soc. Am.* vol. A 36, pp. A20-A33, 2019.

[32] Eric P. Magee and Amy N. Ngwele. *ATMTools: A Toolbox for Atmospheric Propagation and Engagement Geometry Modeling*. MZA Associates Corporation, Version 2018b.1953.

[33] B. M. Welsh. "A fourier series based atmospheric phase screen generator for simulating anisoplanatic geometries and temporal evolution," *Proc. SPIE*, vol. 3125, 1997.

[34] M. Cetin and W. C. Karl. "Feature-enhanced synthetic aperture radar image formation based on nonquadratic regularization," *IEEE Transactions on Image Processing*, vol. 10, no. 4, pp. 623–631, Apr 2001.

[35] L. A. Gorham and Li. J. Moore. "Sar image formation toolbox for matlab," *Proc. SPIE*, vol. 7699, pp. 769906–769906–13, 2010.

[36] S. M. Kay. *Fundamental of Statistical Signal Processing: Estimation Theory*. Prentice-Hal, Englewood Cliffs N.J., 1993.

[37] K. L. Bell and H. L. Van Trees. *Bayesian Bounds For Parameter Estimation and Nonlinear Filtering/Tracking*. IEEE Press, Wiley-Interscience, John Wiley & Sons, Inc., 2007.

[38] R. J. Noll. "Zernike polynomials and atmospheric turbulence∗," *J. Opt. Soc. Am.*, vol. 66, no. 3, pp. 207–211, Mar 1976.

[39] M. S. Pedersen and K. B. Petersen. *The Matrix Cookbook*. matrixcookbook.com. Nov. 2012.

[40] R. van de Geijn and M. Myers. *Advanced Linear Algebra: Foundations to Frontiers*. https://www.cs.utexas.edu/users/flame/laff/alaff-beta/chapter01-norms-matrix-submultiplicative.html

[41] P. Fricker. Zernike Polynomials, MATLAB Central File Exchange. 2020. www.mathworks.com/matlabcentral/fileexchange/7687-zernike-polynomials